Supporting Information: Active Sulfur Sites in Semimetallic Titanium Disulfide Enable CO_2 Electroreduction

Abdalaziz Aljabour,[†] Halime Coskun,[†] Xueli Zheng,[‡,⊥] Md Golam Kibria,[‡,#] Moritz Strobel,[¶] Sabine Hild,[¶] Matthias Kehrer,[§] David Stifter,[§] Edward H. Sargent,[‡] and Philipp Stadler*[,†,‖,‡]

†*Institute of Physical Chemistry, Johannes Kepler University Linz, Altenbergerstrasse 69, 4040 Linz, Austria*

‡*Edward S. Rogers Sr. Department of Electrical and Computer Engineering, University of Toronto, 10 King's College Road, Toronto, Ontario M5S 3G4, Canada*

¶*Institute of Polymer Science, Johannes Kepler University Linz, Altenbergerstrasse 69, 4040 Linz, Austria*

§*Center for Surface and Nanoanalytics, Johannes Kepler University Linz, Altenbergerstrasse 69, 4040 Linz, Austria*

‖*Linz Institute of Technology, Johannes Kepler University Linz, Altenbergerstrasse 69, 4040 Linz, Austria*

⊥*Current address: Department of Materials Science and Engineering, Stanford University, Stanford, CA 94305, USA*

#*Current address: Department of Chemical and Petroleum Engineering, University of Calgary, 2500 University Drive, NW Calgary, Alberta T2N 1N4, Canada*

E-mail: *philipp.stadler@jku.at

Content

Electrical characterization

In the body text we show the electrical resistivities ρ and the carrier concentration n_e of TiS_2 grown by atomic vapor deposition (ALD).[S1–S3] Here is an overview of the detailed electrical parameters obtained by Hall measurements: These are a schematic of the specimen and the resulting geometric factors from the van-der-Pauw measurement (Figure SS1a), the Hall voltage V_H and Hall constant R_H (Figure SS1b) as well as the Hall mobility μ_H (Figure SS1c). For the van der Pauw specimen we deposit 200 nm of TiS_2 by ALD onto a cleaned $1\,\mathrm{x}\,1\,\mathrm{cm}^2$ glass substrate with gold point contacts on each edge. For this we derived all Hall parameters and the resistivity.

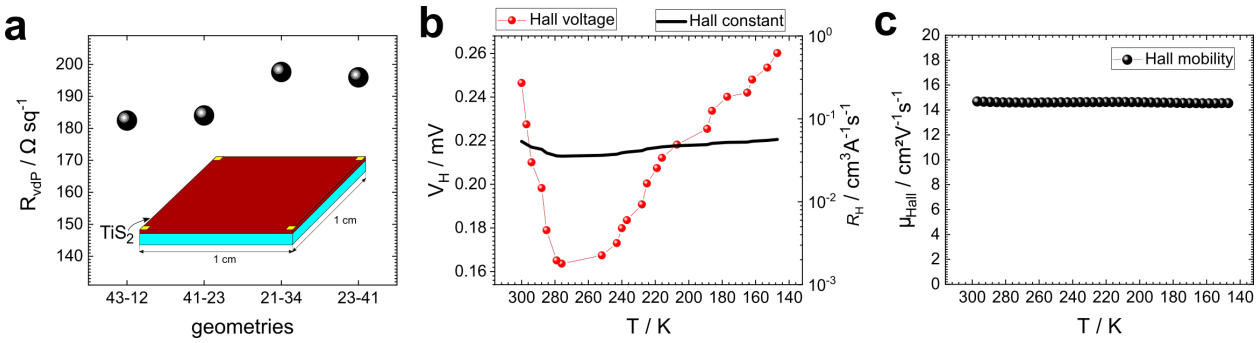

Figure S1: **Hall parameters of 200nm TiS2 film.** (a) Sheet resistivity in a $1\,\mathrm{x}\,1\,\mathrm{cm}^2$ Hall van-der-Pauw specimen. (b) The Hall voltage V_H and Hall constant R_H as function of the temperature T (measured at $100\,\mu$A and 0.91 T magnetic field). (c) Mobility μ_H as function of temperature.

Electrochemical characterization

All electrochemical studies were conducted in a standard three-electrode arrangement in an H-cell configuration (Figure S3). 200 nm of TiS_2 on carbon paper are used to study the electrocatalytic activity (working electrodes, WEs). We use Ni as a counter electrode (CE) to improve the oxygen evolution. For our studies it was necessary to employ a hybrid solvent (acetonitrile and water) to address stability (TiS_2 can hydrolyze in all-aqueous media)[S1] and to improve the solubility of CO_2 (up to $0.2\,\mathrm{mol\,L^{-1}}$). Furthermore, we found the presence of water advantageous to create a continuous electrolysis cycle with co-evolution of O_2 (in addition to CO-evolution on the cathode) on the Ni anode. As such we create an electrolysis CO_2 splitting to CO and O_2 ideal for long-term studies without risk of unwanted side-oxidation of the electrolyte (oxidation of EMIM-BF_4 and NBu_4-PF_6) or the co-solvent (oxidation of CH_3CN). To determine the reference potential we use a calibrated Ag/AgCl quasi reference electrode (QRE). The electrolyte is 0.1 M NBu_4-PF_6 or 4% EMIM-BF_4 in acetonitrile-water. The water amount is set to 1%vol (or, $0.56\,\mathrm{mol\,L^{-1}}$). The reference potential (calibration) of the QRE is measured referring the ferrocene/ferrocenium couple (Fc/Fc^+). We compared the standard potential $E_{QRE\,vs.\,Fc/Fc^+}$ in the CO_2-purged state, in 0.1 M NBu_4-PF_4 or 4% EMIM-BF_4 in acetonitrile-water. The system CO_2, water and CH_3CN and the electrolyte will lead to a constant pH with only negligible changes. From the as-derived $E_{QRE\,vs.\,Fc/Fc^+}$

we calculated the standard reference potentials of the reversible hydrogen electrode (RHE, equation 1:

$$E_{RHE} = E_{QRE\,vs.\,Fc/Fc^+} + 0.641\,V + pH \cdot 0.0591\,V \tag{1}$$

We show the calibration against Fc/Fc^+ (sweeps) inside the cyclic voltammetry plots (body text, Figure 4). The cell parameters/constants and the electrochemical surface area (ECSA) were studied by electrochemical impedance spectroscopy (EIS). Spectra were recorded between 100 mHz and 0.1 MHz with an *ac*-amplitude of 50 mV (Figures SS2 and SS3 and Table SS1). From the Bode-plot we derive the resistances (R_{el}, electrolyte, R_m, membrane/frit) and the working electrode capacitance (C_{WE}). The latter is used to estimate the surface factor of the electrochemical surface area (f_{ECSA} of carbon paper, equation 2) and to calculate the current density (j_{ECSA}) from the projected surface area. As reference capacitance we use $40\mu F\,cm^2$ (planar glassy carbon).[S4]

$$f_{ECSA} = \frac{C_{WE}}{C_{ref}} \qquad j_{ECSA} = \frac{j_{projected}}{f_{ECSA}} \tag{2}$$

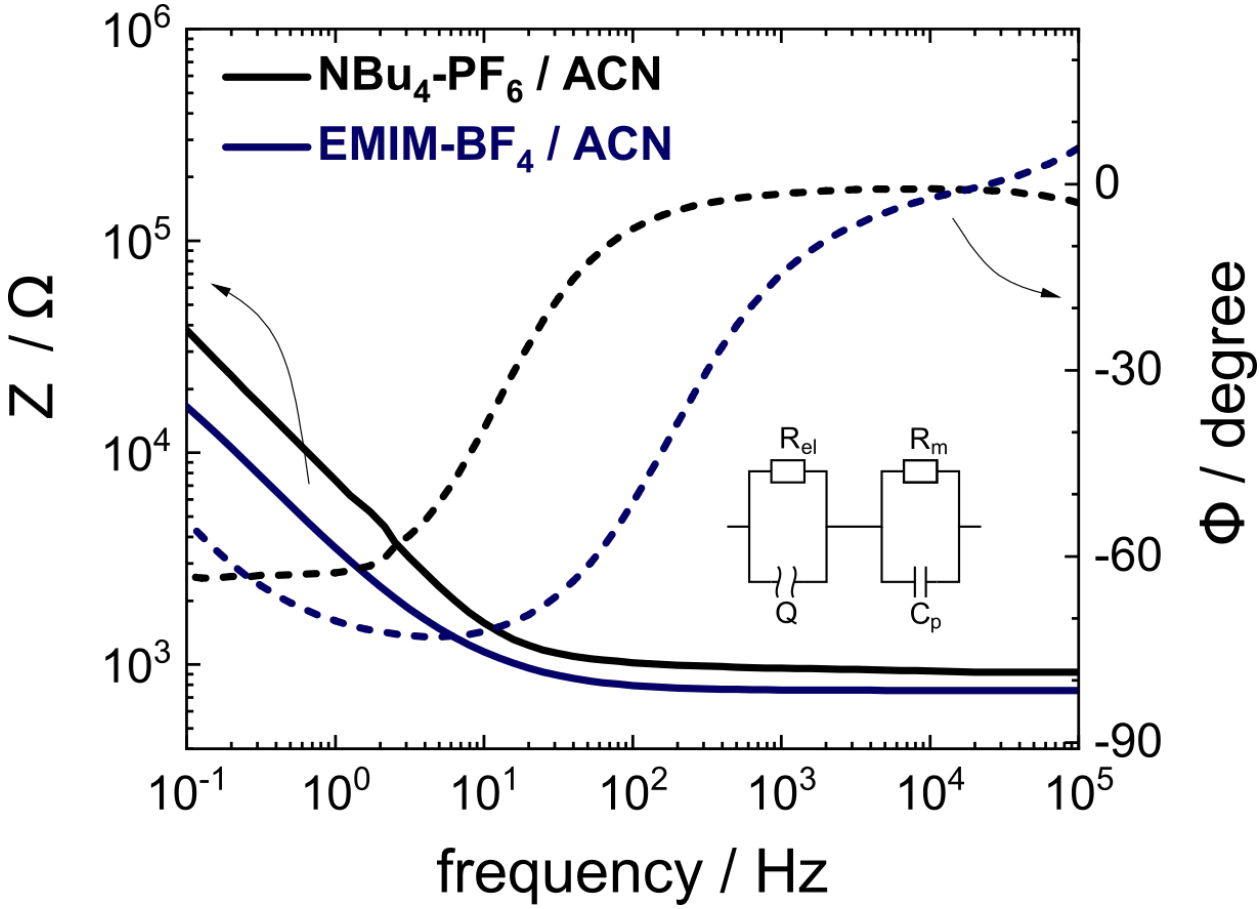

Figure S2: **Impedance data of electrolysis cell in NBu_4-PF_6 and EMIM-BF_4 electrolyte solution.** Bode-plot of the electrolysis cell used to derive the resistances (R_{el} and R_m) and the WE-capacitance (to further calculate the surface factor f_{ECSA}). Inset: (b) Equivalent circuit used to derive the cell constants R_{el}, R_m and C_{WE}. C_{WE} is crosschecked by j vs. scan rate, Figure S3 and used to calculate the ECSA.

Table S1: Cell constants measured from electrochemical impedance spectroscopy; values normalized to 1 cm^2.

electrolyte	WE	CE	R_{el}* / Ω	R_m* / Ω	C_{WE} / μF	f_{ECSA}
0.1 M NBu_4-PF_4	TiS_2	Ni	51.0	$4.82 \cdot 10^4$	186	4.65
4% EMIM-BF_4	TiS_2	Ni	27.5	$1.32 \cdot 10^4$	178	4.45

*electrolyte and membrane resistances

The working electrode capacitance (C_{WE}) was further determined using current density j at different scan rates (Figure S3a). The capacitance is derived at -0.2 V vs. Ag/AgCl QRE by taking the slope from j versus scan rate plot (Figure S3b). From this, we derive a similar capacitance as before measured by electrochemical impedance spectroscopy at 188 $\mu F\,cm^{-2}$.

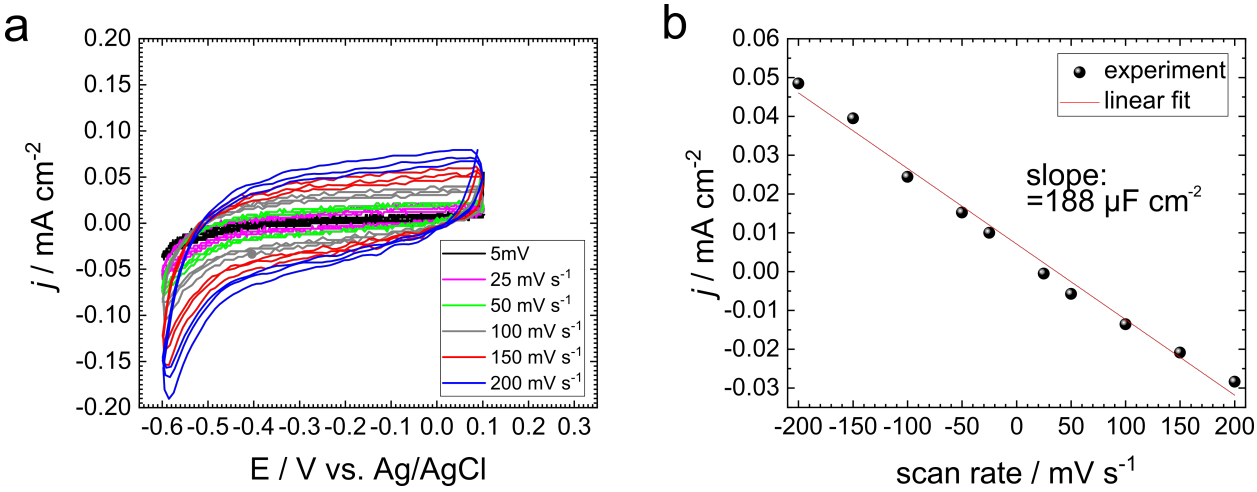

Figure S3: ***j* vs. scan rate to determine the electrochemical surface area.** (a) ECSA-measurement of displacement currents in NBu_4-PF_6 on the working electrode at different scan rates. (b) Plot of the scan rates (taken at -0.2 V vs. Ag/AgCl QRE) versus the current densities j to derive the capacitance C_{WE}. The linear fit (slope) shows a similar value for carbon paper as reported by electrochemical impedance spectroscopy ($C_{WE} = 188\,\mu F\,cm^{-2}$).

Water and conductivity

In addition, we explored the effect of water on the ionic conductivity. The Bode-plot (Figure SS4) shows only a minor decrease of R_{el} between 1 and 10%$_{vol}$ water (52.4 $\Omega\,cm^{-2}$ and 50.1 $\Omega\,cm^{-2}$, respectively).

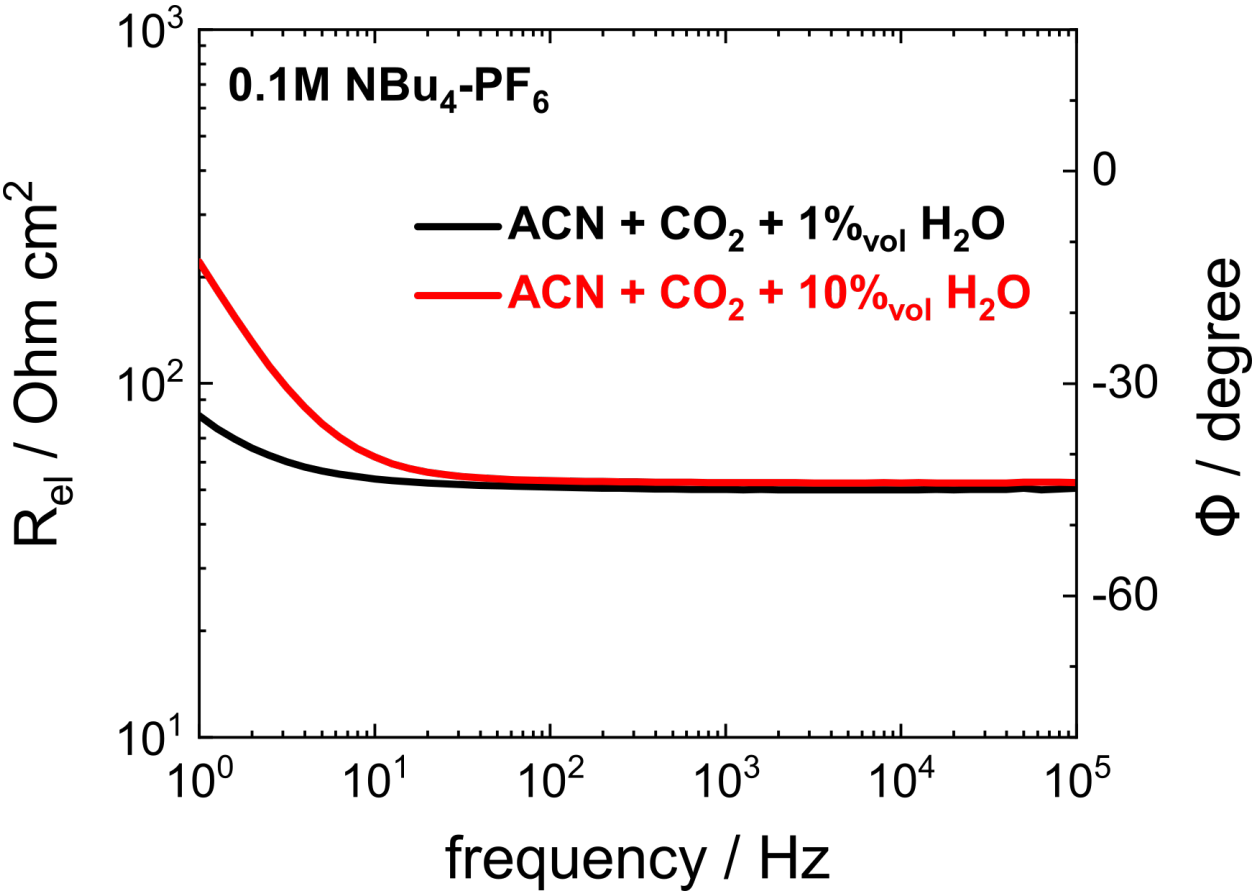

Figure S4: **R_{el} in NBu_4-PF_6 at 1% and 10% water content.** Bode-plot of R_{el} shows little effect of water on the electrolyte conductivity (*i.e.* decrease of R_{el} from ($52.4\,\Omega\,cm^{-2}$ to $50.1\,\Omega\,cm^{-2}$).

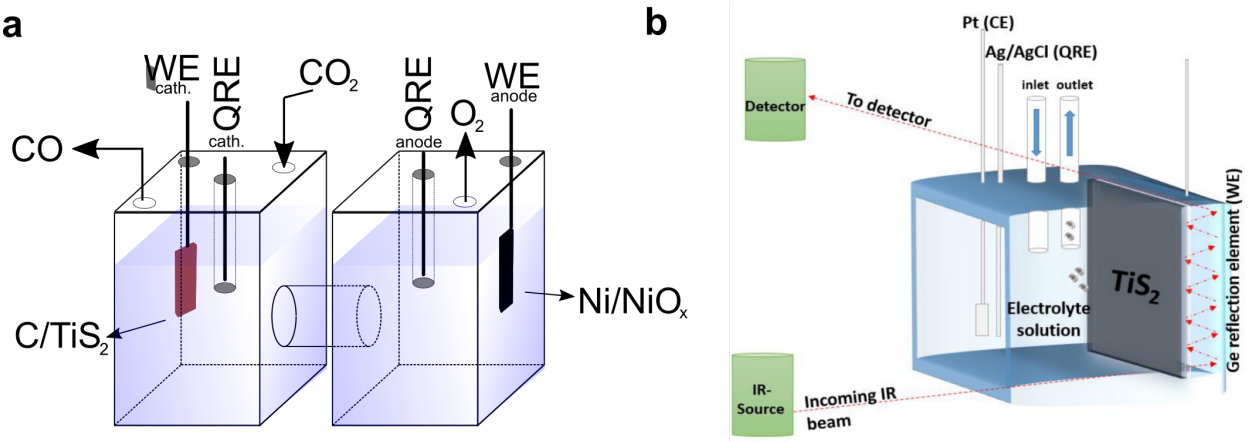

Figure S5: **Schematic of the cells used to study CO_2-splitting to CO and O_2.** (a) Electrolysis cell: For the anode side, a Ni/NiO_x counter electrode (CE) is employed to activate the evolution of O_2 and to suppress unwanted degradation of the electrolyte and solvent.[S5–S7] (b) Spectroelectrochemical flow cell: Schematic of the in-situ ATR-FTIR internal reflection mode to explore the stability/mechanism of CO_2RR on TiS_2.

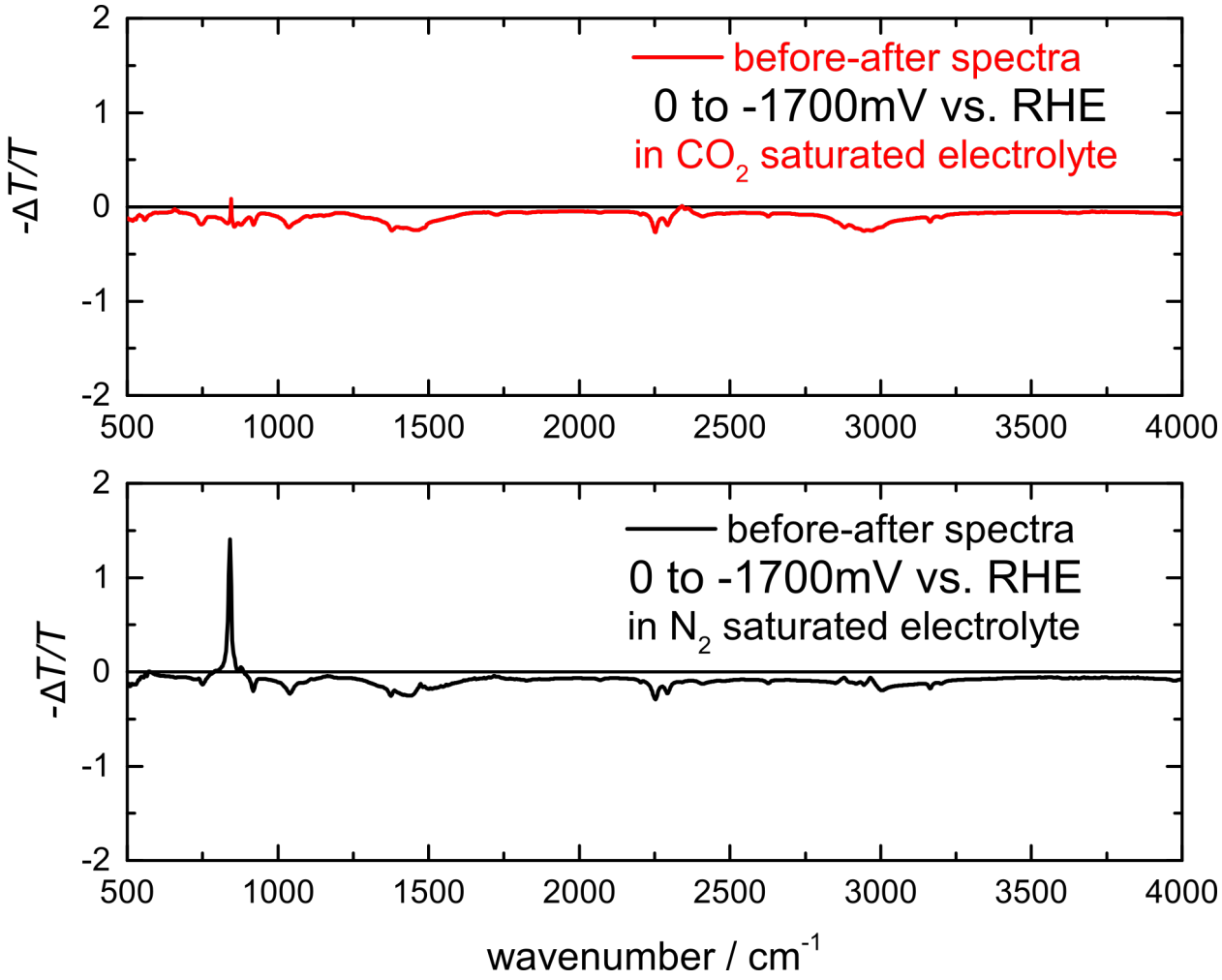

Figure S6: **In-situ ATR-FTIR spectroscopy employed to explore stability/reversibility.** Scan to maximum reduction potential (-1.7 V vs. RHE) and back (before-after-scan) in N_2 saturated and CO_2 saturated environment. In both cases, the response from TiS_2 shows the spectroscopic fingerprints of CH_3CN and the electrolyte (NBu_4-PF_6) and, in presence of CO_2, accumulation of CO_2 on the surface.

In-situ FTIR

The scheme/function of the in-situ FTIR setup is depicted in Figure S5b: It comprises *(i)* a germanium parallelepiped serving as the infrared reflection element for attenuated total reflection mode (ATR), *(ii)* the electrocatalysts (200 nm TiS_2) deposited on top of this element, *(iii)* the flow-cell mounted onto the reflection element and *(iv)* the electrical and solution supply tubes. The entire flow cell is made from Teflon. The feedthroughs for the tubes are tightened using wax. The cell is placed into the FTIR-probe space onto a custom designed holder. We tighten the cell using a Teflon bolt and a rubber o-ring between flow-cell and germanium-TiS_2. The electrical contacts are provided by thin copper wires outside the FTIR-setup. During measurement we continuously supply fresh CO_2-saturated electrolyte and measure the IR-response as function of time and electrochemical potential (and current). The ATR-mode delivers a qualitative insight to the surface reactions related to CO_2RR. In addition we see accumulation/depletion of the electrolyte and solvent. The estimated penetration depth of the evanescent wave is a few µm at the interface TiS_2/electrolyte. Quantitative estimations have to be considered with care, since the penetration depth is also dependent on the wavelength. We subsequently interpret our spectra only surface- and near-surface-sensitive (*i.e.* adsorption on the surface and adjacent Helmholtz-layer on the TiS_2/solution interface). The difference spectra -ΔT and differential spectra -ΔT/T depict the changes experimentally observed within these layers. Bulk changes in TiS_2 (massive degradation or dissolution/degradation from the electrode) can be clearly excluded within the reported potential window between 0 and -1720 mV vs. RHE (Figure SS6).[S8–S10] All changes seen in this stability scans relate either to the electrolyte, the acetonitrile and, in CO_2-saturated solution, to CO_2. Above these potential windows we cannot exclude the dissolution/reaction of the electrocatalyst and the germanium with the corresponding electrolyte.

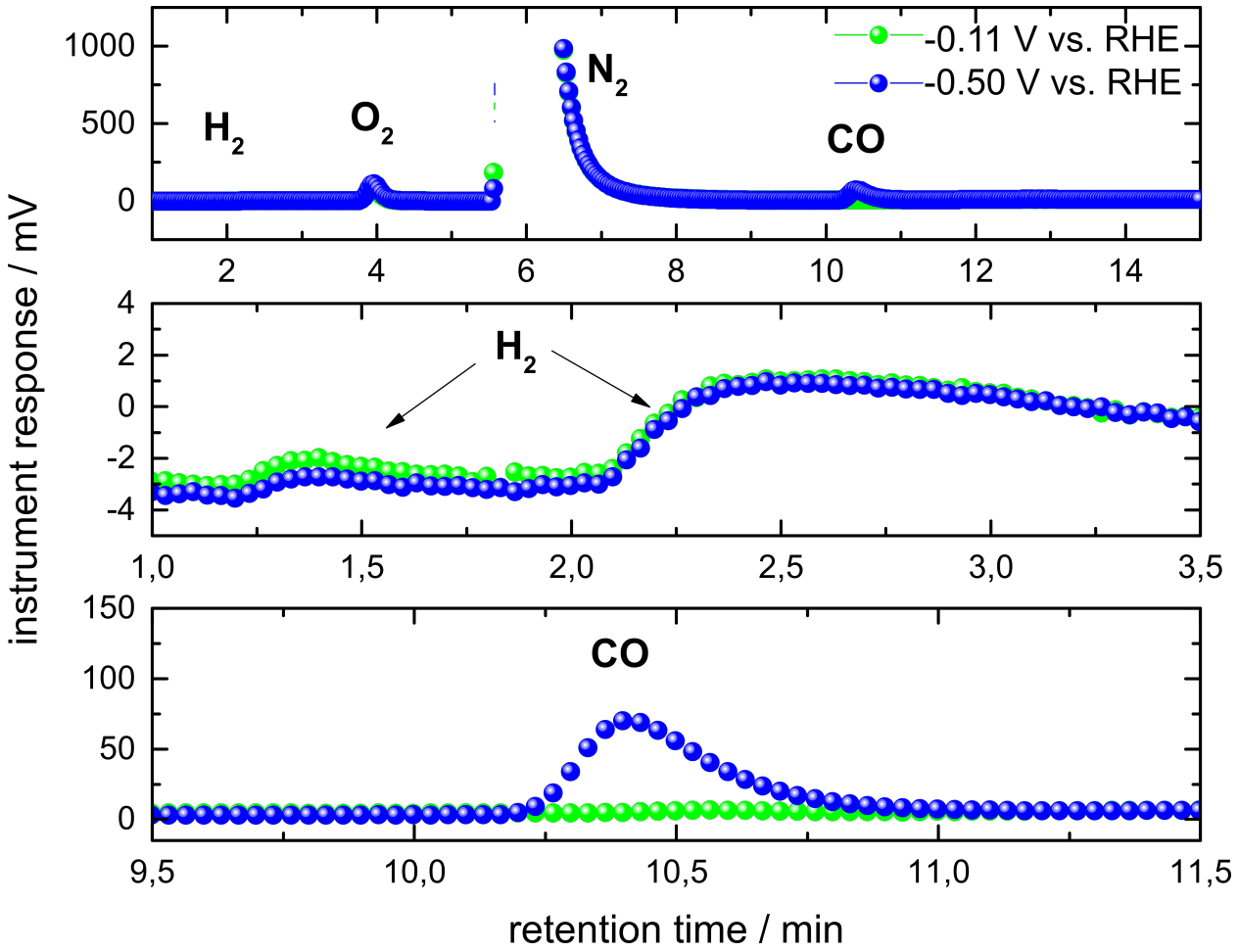

Figure S7: **Analysis of CO_2RR products in the head space.** Gas chromatograms show the gaseous product distribution at -0.11 V vs. RHE (zero overpotential for CO, reference scan with hydrogen evolution). At -0.5 V vs. RHE (or 0.39 V overpotential) we detect a similar amount of H_2 and preponderantly evolution of CO.

Chromatographic CO detection

From chronoamperometric scans we detected the onset of CO evolution and the quantitative determination of CO to calculate the Faradaic efficiencies. We present that at the reported onset for CO evolution at $5\,mA\,cm^{-2}$ at -0.5 V vs. RHE (or 0.39 V overpotential), a distinct CO peak appears (correlating to 83% Faradaic yield). At the thermodynamic equilibrium for CO evolution (-0.11 mV vs. RHE), only hydrogen is detected. The hydrogen content (and as such j_{H_2}) remains approximately constant between -0.11 and -0.5 mV vs. RHE (nn) which underlines the selectivity of TiS_2 for CO.

Addendum: Mechanistics

As proposed in Figure 3a,b (body text), we further show the difference spectra in the thiole fingerprint regime (S-H bonding) that emerges between 1550-1590 cm^{-1}. Similar features have been reported for MoS_2[S11] for hydrogen evolution. We indicate this analogy in the differnce scan, since a minor fraction of our product is also hydrogen (Figure SS8).

Addendum: Comparison

Ag and Au (thin films on glass by physical vapor deposition) are compared to TiS_2 using the same electrolyte (NBu_4-PF_6) (Figure SS9).

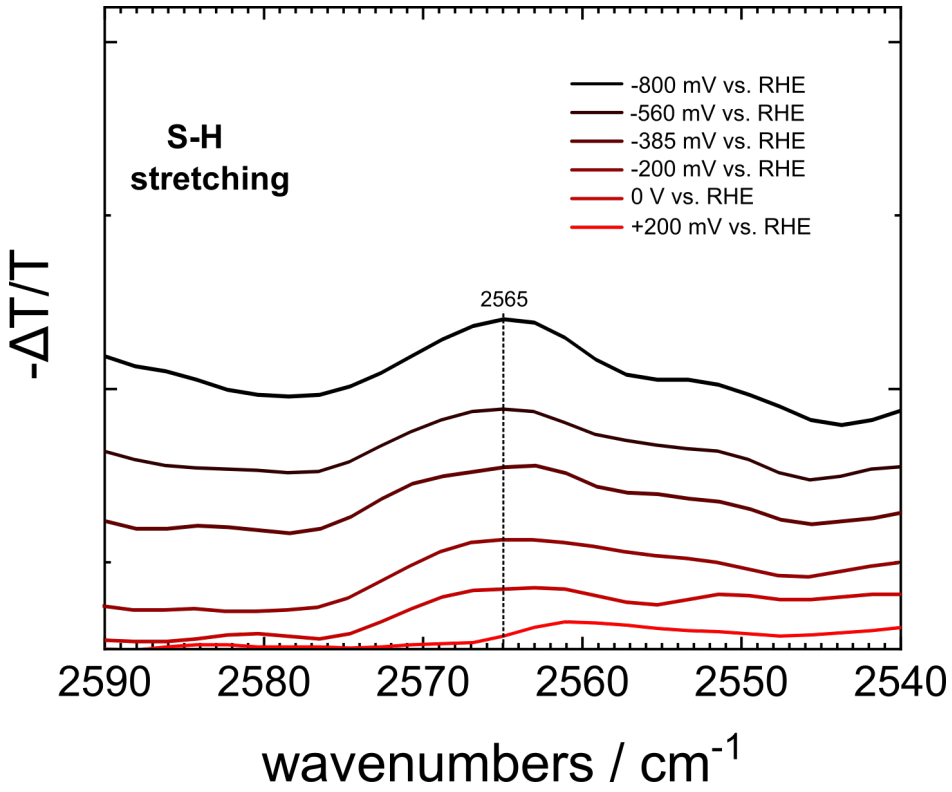

Figure S8: **Fingerprint regime for thiole in the differential scan of the in-situ ATR-FTIR system**. The spectra reveal a distrinct S-H stretching at 1565 cm^{-1} upon increasing cathodic bias (co-evolution of hydrogen besides CO).

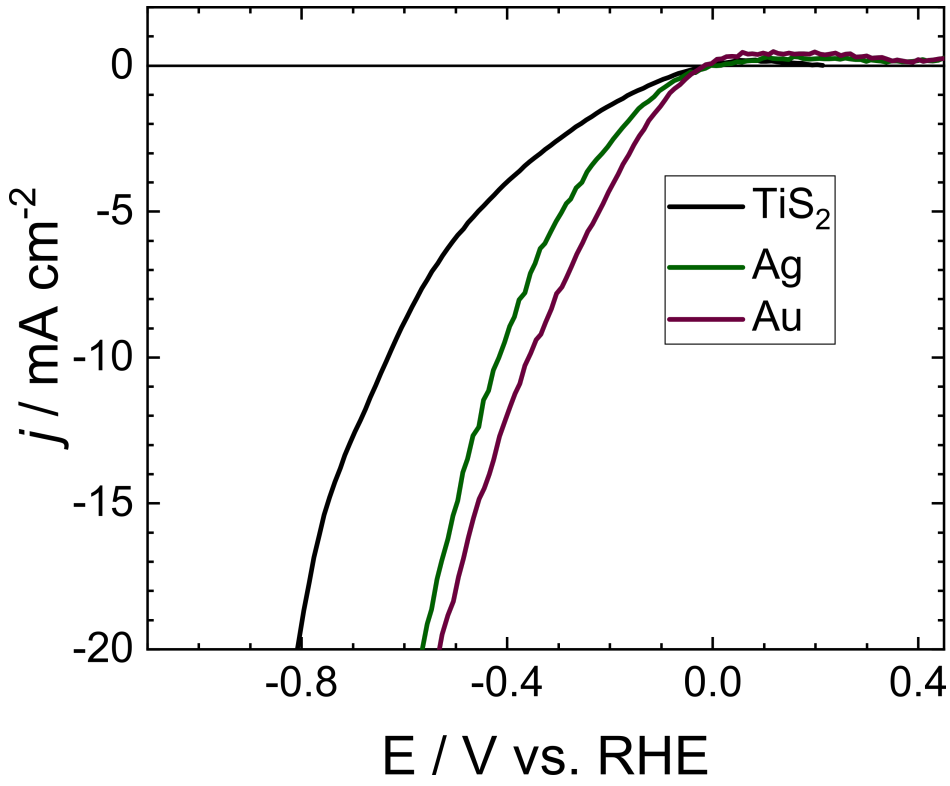

Figure S9: **Voltammograms of Au, Ag and TiS_2 in the same electrolyte for comparison.**

References

(S1) Cucinotta, C. S.; Dolui, K.; Pettersson, H.; Ramasse, Q. M.; Long, E.; O'Brian, S. E.; Nicolosi, V.; Sanvito, S. Electronic Properties and Chemical Reactivity of TiS 2 Nanoflakes. *The Journal of Physical Chemistry C* **2015**, *119*, 15707–15715.

(S2) Whittingham, M.; Panella, J. A. Formation of stoichiometric titanium disulfide. *Materials Research Bulletin* **1981**, *16*, 37–45.

(S3) Conroy, L. E.; Park, K. C. Electrical properties of the Group IV disulfides, titanium disulfide, zirconium disulfide, hafnium disulfide and tin disulfide. *Inorganic Chemistry* **1968**, *7*, 459–463.

(S4) Ji, H.; Zhao, X.; Qiao, Z.; Jung, J.; Zhu, Y.; Lu, Y.; Zhang, L. L.; MacDonald, A. H.; Ruoff, R. S. Capacitance of carbon-based electrical double-layer capacitors. *Nature Communications* **2014**, *5*, 3317.

(S5) Aljabour, A.; Apaydin, D. H.; Coskun, H.; Ozel, F.; Ersoz, M.; Stadler, P.; Sariciftci, N. S.; Kus, M. Improvement of Catalytic Activity by Nanofibrous CuInS 2 for Electrochemical CO 2 Reduction. *ACS Applied Materials & Interfaces* **2016**, *8*, 31695–31701.

(S6) Aljabour, A.; Coskun, H.; Apaydin, D. H.; Ozel, F.; Hassel, A. W.; Stadler, P.; Sariciftci, N. S.; Kus, M. Nanofibrous cobalt oxide for electrocatalysis of CO 2 reduction to carbon monoxide and formate in an acetonitrile-water electrolyte solution. *Applied Catalysis B: Environmental* **2018**, *229*, 163–170.

(S7) Adam, G.; Aslan, F.; Portenkirchner, E.; Stadler, P.; Scharber, M. C.; Sariciftci, N. S. Electrocatalytic Reduction of Carbon Dioxide using Sol-gel Processed Copper Indium Sulfide (CIS) Immobilized on ITO-Coated Glass Electrode. *Electrocatalysis* **2015**, *6*, 405–413.

(S8) Coskun, H.; Aljabour, A.; De Luna, P.; Farka, D.; Greunz, T.; Stifter, D.; Kus, M.; Zheng, X.; Liu, M.; Hassel, A. W.; Schöfberger, W.; Sargent, E. H.; Sariciftci, N. S.; Stadler, P. Biofunctionalized conductive polymers enable efficient CO 2 electroreduction. *Science Advances* **2017**, *3*, e1700686.

(S9) Zheng, X.; De Luna, P.; García de Arquer, F. P.; Zhang, B.; Becknell, N.; Ross, M. B.; Li, Y.; Banis, M. N.; Li, Y.; Liu, M.; Voznyy, O.; Dinh, C. T.; Zhuang, T.; Stadler, P.; Cui, Y.; Du, X.; Yang, P.; Sargent, E. H. Sulfur-Modulated Tin Sites Enable Highly Selective Electrochemical Reduction of CO 2 to Formate. *Joule* **2017**, *1*, 794–805.

(S10) Enengl, C.; Enengl, S.; Havlicek, M.; Stadler, P.; Glowacki, E. D.; Scharber, M. C.; White, M.; Hingerl, K.; Ehrenfreund, E.; Neugebauer, H.; Sariciftci, N. S. The Role of Heteroatoms Leading to Hydrogen Bonds in View of Extended Chemical Stability of Organic Semiconductors. *Advanced Functional Materials* **2015**, *25*, 6679–6688.

(S11) Tsai, C.; Li, H.; Park, S.; Park, J.; Han, H. S.; Nørskov, J. K.; Zheng, X.; Abild-Pedersen, F. Electrochemical generation of sulfur vacancies in the basal plane of MoS2 for hydrogen evolution. *Nature Communications* **2017**, *8*, 1–8.